Review of Scientific Instruments

RESEARCH ARTICLE | SEPTEMBER 16 2024

The development of a low-temperature terahertz scanning tunneling microscope based on a cryogen-free scheme

Huaiyu Zhang; Dacheng Tian; Yang Zhan; Zijia Liu; Chen Ma; Yuwu Zhang; Jianwei Hu; Xiaoyue He; Baojie Feng; Yiqi Zhang; Lan Chen; Peng Cheng; Kehui Wu

Rev. Sci. Instrum. 95, 093703 (2024)
https://doi.org/10.1063/5.0208689

Review of Scientific Instruments ARTICLE pubs.aip.org/aip/rsi

The development of a low-temperature terahertz scanning tunneling microscope based on a cryogen-free scheme

Cite as: Rev. Sci. Instrum. 95, 093703 (2024); doi: 10.1063/5.0208689
Submitted: 16 March 2024 • Accepted: 28 August 2024 •
Published Online: 16 September 2024

View Online Export Citation CrossMark

Huaiyu Zhang,[1,2] Dacheng Tian,[1,2,3] Yang Zhan,[1,2] Zijia Liu,[1,2,3] Chen Ma,[1,2,3] Yuwu Zhang,[3] Jianwei Hu,[3] Xiaoyue He,[3] Baojie Feng,[1,2] Yiqi Zhang,[1,2] Lan Chen,[1,2] Peng Cheng,[1,2,a)] and Kehui Wu[1,2,3,a)]

AFFILIATIONS

[1] Institute of Physics, Chinese Academy of Sciences, Beijing 100190, China
[2] School of Physical Sciences, University of Chinese Academy of Sciences, Beijing 100049, China
[3] Songshan Lake Materials Laboratory, Dongguan, Guangdong 523808, China

[a)] Authors to whom correspondence should be addressed: pcheng@iphy.ac.cn and khwu@iphy.ac.cn

ABSTRACT

We have developed a cryogen-free, low-temperature terahertz scanning tunneling microscope (THz-STM). This system utilizes a continuous-flow cryogen-free cooler to achieve low temperatures of ~25 K. Meanwhile, an ultra-small ultra-high vacuum chamber results in the reduction of the distance from sample to viewport to only 4 cm. NA = 0.6 can be achieved while placing the entire optical component, including a large parabolic mirror, outside the vacuum chamber. Thus, the convenience of optical coupling is much improved without compromising the performance of STM. Based on this, we introduced THz pulses into the tunnel junction and constructed the THz-STM, achieving atomic-level spatial resolution in THz-driven current imaging and sub-picosecond (sub-ps) time resolution in autocorrelation signals during pump–probe measurements. Experimental data from various representative samples are presented to showcase the performance of the instrument, establishing it as an ideal platform for studying non-equilibrium dynamic processes at nanoscale.

I. INTRODUCTION

The nature of quantum-tunneling electrons enables the scanning tunneling microscope (STM) to achieve impressive high spatial resolution, making it an indispensable tool for investigating surface atomic structures and electronic states. However, the STM's temporal resolution is a drawback as a single scan typically takes several minutes. Consequently, ongoing research efforts are devoted to improving the STM's capabilities to achieve both outstanding spatial and temporal resolutions.[1]

One of the primary approaches being explored is the development of high-speed STM. Typically, the scanning rate of STM is influenced by factors such as the sampling rate, circuit bandwidth (BW), the feedback system, and the response time of the scanning piezo-tube. The sampling rate and the circuit BW are limited to the intermediate frequency (IF). Higher scanning rates result in a reduction in the number of samples per pixel or the number of pixels per unit area. Furthermore, the tunnel junction has a mechanical resonance frequency, and achieving higher scanning rates requires more sensitive feedback, while sensitive feedback can easily lead to resonance. In addition, the scanning piezo-tube exhibits a time delay in response to applied voltage, causing significant distortion in collected images at high scanning rates. Recent developments have enabled fast scanning STMs to achieve frame rates of several hundred frames per second, proving their value in studying surface diffusion, reconstruction, and aggregation of atoms, clusters, or molecules. Notably, these dynamic processes, which lack a defined starting time, are difficult to investigate directly through the pump–probe technique. Thus, fast scanning STM remains an irreplaceable tool in such research works.[2,3]

The introduction of pump–probe technique provides an alternative approach to conduct time-resolved measurements in STM. This technique involves acquiring the tunneling current signal at varying time delays between the pump and probe pulses. Although a time resolution on the order of nanosecond (ns) can be achieved with electric pulses applied directly onto the junction in a radio frequency (RF) circuit, optical pulses are preferred in order to overcome the limitations of the circuit's BW. For instance, Weiss *et al.* demonstrated an early example of achieving picosecond (ps) resolution by using two sets of laser pulses to separately gate the bias wire and the current wire, with controlled time delay between them.[4] To avoid the constraints imposed by electric wires, researchers have employed a method where optical pulses are directed at the junction to achieve sub-picosecond (sub-ps) time resolution. However, this approach introduces a complex interaction between the optical pulses and the tunnel junction. Apart from the optical rectification effect, various nonlinear effects can occur, including nonlinear effects such as the excitation of high-energy phonons (known as the photothermal effect), which cannot be eliminated using conventional techniques such as choppers and lock-in amplifiers (LIA).[5,6]

The combination of STM with terahertz (THz) pump–probe techniques shows promise in avoiding such complexities while maintaining ultrafast temporal resolution, leading to the development of THz-STM. The first THz-STM was invented by Tyler *et al.* in 2013 in Hegmann's group,[7] on which THz-driven rectified current was collected on Au nanoislands and optical pump–THz probe experiment was performed on InAs nanodots. All the experiments were performed in air at that time, but soon a THz-STM work under ultra-high vacuum (UHV) was reported,[8] in which THz-driven current on pentacene molecules was recorded and an oscillation of the current signal during THz pump–THz probe was observed, which is attributed to the vibration of the molecules. After that in 2020, they achieved coherent control over the switch of an individual MgPc molecule using THz-driven current.[9,10] In addition to molecules, solid surfaces have been investigated using THz-STM as well. The first atomic resolution of THz-driven current on Si(111) 7×7 reconstruction was reported in 2017[11] and the behavior of the driven current on Cu(111) was comprehensively studied in 2020,[12] both by Hegmann's group. Takeda's group reported the performance of their THz-STM in 2016,[13] and in 2018, they were the first to introduce a continuous phase shifter for the THz waveform, allowing for the carrier-envelope phase-control.[14] By 2020, they had developed THz-field-driven scanning tunneling luminescence (THz-STL) spectroscopy, a technique that impressively combined THz-STM and STL, and achieved an upconversion of the photon energy.[15] In addition, Wilson's group has focused on the THz rectification spectroscopy (TRS), demonstrating its comparability with the inelastic electron Tunneling spectroscopy (IETS) signal. Recently, they reported a series of works on the dynamics of single H_2 or CO molecule inside the tunneling junction using THz-STM,[16–20] serving as a quantum sensor. Other systems, such as Au(111) surface[21,22] and C_{60} island,[23,24] were also studied by other research groups.

THz-driven current generation can be easily explained: the electric field component is oriented perpendicular to the sample surface, creating a transient voltage between the tip and the sample, thereby inducing a transient tunneling current. Compared to other kinds of optical pulses, THz pulses carry less energy and typically stimulate a limited number of quasiparticles, making them advantageous for experimental data analysis. There are primarily two different response times in the STM junction: the average traversal time for individual electrons and the collective response time, which is represented by the plasma modes of the junction acting as a resonant cavity. The traversal time for a tunneling electron is estimated to be around 10^{-16} s, as suggested by both theoretical calculations and experimental results.[25–27] On the other hand, the tip-enhanced Raman scattering (TERS)[28] and the STM-induced luminescence (STML)[29] involve wavelengths within the visible spectrum, indicating a characteristic time for collective modes of $\sim 10^{-15}$ s. These time scales are significantly shorter than the period of the THz pulse, suggesting that the THz photons lack sufficient energy to activate these excitations. Hence, the THz electric field can be approximated as a quasi-static bias for the tunneling electrons.

THz pulses can be considered as bundles of photons, each carrying energy levels in the milli-electron volt (meV) range, capable of generating excitations within this energy range. The characteristics of a THz pulse, such as its pulse width and spectrum, have a direct impact on its time and energy resolution. A narrower pulse width generally leads to higher time resolution but may result in lower energy resolution due to its wider spectrum. Conversely, a wider pulse width reduces time resolution, but offers more precise excitation energy due to a narrower spectrum. Currently, most reported THz-STM systems treat THz pulses as a transient bias; therefore, single-cycle THz pulses are chosen,[8–18,20–24,30–38] while TRS is practically achieved using continuous-wave THz-STM.[19] In order to focus the THz pulses into the junction, the use of a parabolic mirror can be advantageous as it allows independent reflection regardless of refractivity, in contrast to lenses. Nevertheless, incorporating a parabolic mirror in the UHV chamber requires precise adjustments of numerous degrees of freedom.

In this paper, we present our home-built THz-STM system, where we have made several advancements. Instead of a bulky static liquid helium dewar, we utilize a continuous-flow cryogen-free cooler to achieve low temperatures, resulting in a significant reduction in the size of the ultra-high vacuum (UHV) chamber. Consequently, the distance from sample to the optical viewport is reduced to about 4 cm, and a numerical aperture (NA) as large as 0.6 is accessible from the viewport. By positioning the focusing parabolic mirror outside the chamber, the THz light beams are focused at the STM tunneling junction. We verified the performance of our THz-STM system through a series of experiments. In the following, we first describe the setup of our system, including the STM module and the THz module, as well as the coupling of these two parts. We will then present some typical experimental results obtained using our THz-STM to demonstrate the performance of our system.

II. EXPERIMENTAL SETUP

A. The LT-UHV-STM part

The low-temperature environment of our LT-STM is achieved through a commercial continuous-flow cryogen-free cooler (Qcryo, Physike Co., China) that operates in two cycles.[39] In the first cycle, a Gifford–McMahon (GM) cryocooler cools down two stages of cold heads, allowing for heat exchanges with the second cycle. In the second cycle, the helium is continuously pumped into a cryostat located inside the STM chamber through a flexible corrugated pipe. By controlling the needle-valve and employing the Joule-Thomson (JT) refrigeration and the adiabatic expansion of helium, the cryostat cold head is further cooled, ultimately reaching a temperature of 2.5 K. The scanner is suspended under the cryostat cold head directly with beryllium-copper springs and an oxygen-free copper braid. To shield the scanner from thermal radiation and electromagnetic interference, it is enveloped by a dual-layered thermal shield mounted on the cryostat cold head. A hole is positioned on the shields to allow optical beams to pass through. To facilitate optical alignment and provide convenience, the cryostat cold head is connected to a four-dimensional positioning stage. This stage enables adjustments of displacement with a traveling precision of 0.002 mm and maximum traveling length of 12 mm each, and the z direction has a traveling precision of 0.2 mm and maximum traveling length of 100 mm as well as tilt angles within an angle of ~±5°, allowing the scanner to move accordingly. The entire vacuum chamber is situated on a pair of active-damping modules to isolate the vibrations from the building or other mechanical noise transmitted from the floor in three dimensions.

The STM scanner is purposefully designed to offer openness, ensuring integration with optical components. The STM scanner has a modified Pan-type configuration, with the magnets for the eddy current damping positioned in a circular arrangement around it. Due to the small diameter of the cryostat cold head (only 2 cm) (Fig. 1), the STM scanner is designed with a remarkable compactness. The UHV chamber itself is also compact, with just a 4 cm distance from the flange entrance to the STM tip. Therefore, it is easy to achieve focus by placing the parabolic mirror outside the UHV chamber. This design scheme significantly enhances the convenience of optical coupling.

The STM system is equipped with a preparation chamber that allows for the processing of samples in various ways. Within this chamber, samples can be heated up to 800 °C through a tungsten filament radiation and can be further heated up to 1500 °C by e-beam heating. An argon gun is equipped to bombard to the sample surface, and a variety of evaporation sources aiming at the sample stage can be used for molecular beam epitaxy (MBE). Moreover, a cleavage stage is incorporated to enable cleaving of bulk materials and obtain clean sample surfaces.

B. The THz optical part

The schematic of the whole optical path is shown in Fig. 2. The femtosecond (fs) laser used in this setup is a CARBIDE model from Light Conversion Co., with a wavelength centered at 1030 nm. The linearly polarized pulses emitted by the laser are divided into four beams, each of which is directed to its respective delay line stage. These stages are utilized to manipulate the relative time delay between the beams.

Two of the beams are specifically employed to generate THz pulses. This is accomplished by directing the beams through a grating and subsequently focusing them onto a $LiNbO_3$ crystal at a specific angle to meet the phase-matching condition, according to the tilted-wavefront method. This method offers several advantages. First, it allows for the generation of relatively high-powered THz pulses, which is desirable for effectively driving current. In addition, the generated THz pulses and the residual 1030 nm pulses go non-collinear after passing through the crystal, which is convenient for collecting THz pulses. The repetition rate of our fs laser is 1 MHz, and its maximum output power is 20 W. The energy conversion efficiency of the THz pulses in our system can reach 0.5‰.

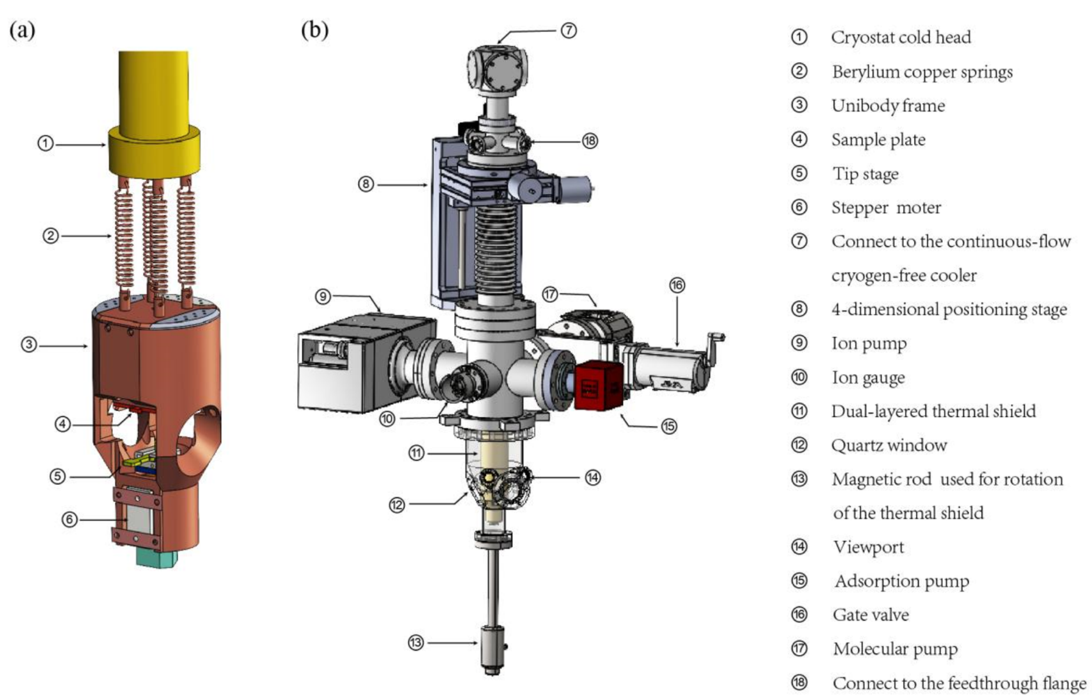

FIG. 1. (a) Structure of the STM scanner suspended under the cryostat cold head. (b) Structure of the UHV-STM chamber.

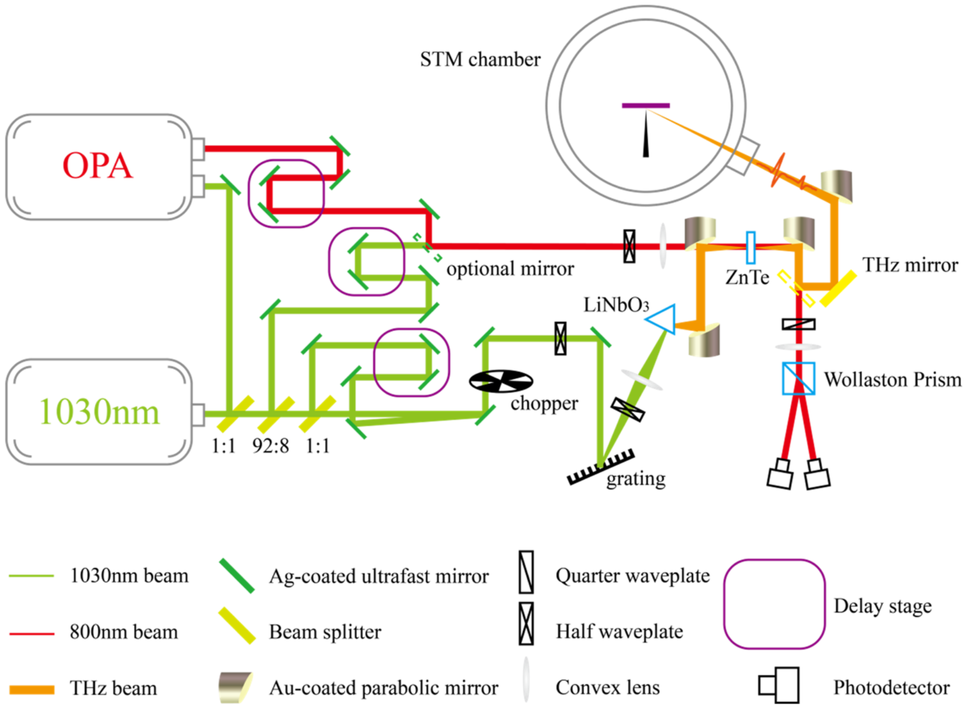

FIG. 2. Schematic of the generation and sampling of the THz pulses and their coupling with STM.

The two beams of 1030 nm pulses each generate a beam of THz pulses, which are emitted nearly in the same direction and propagate along the same path. In order to prevent interference between the two beams, they are separated at a small angle of ~0.15°. Compared to the Michelson–Morley (MM) interferometer scheme, this method eliminates the need for a THz beam splitter, which prevents any loss of energy or changes in the waveform of the THz pulses. However, a disadvantage of this method is that the conversion efficiency of one of the THz beams will decrease due to deviation from the strict phase-matching condition. Fortunately, the experimental results suggest that the power of the THz pulses is sufficient for driving tunneling current.

Each time the THz pulses pass through a node on a mirror or a focal point, they undergo half-wave loss. We can reverse the phase of the THz pulses by a pair of TPX lenses with a common focal length of 50 mm, which is known as the Gouy phase shift. Furthermore, the polarization of the THz pulses can be continuously adjusted by grid polarizers, and the power of the transmitted THz pulses varies with the direction of a polarizer in accordance with the Malus law (1), where I_0 is the intensity of the incident light, I is the intensity of the transmitted light, and θ is the angle between the direction of the polarization of the incident light and the direction of the polarizer,

$$I = I_0 \cos^2\theta. \tag{1}$$

The third 1030 nm beam first passes through a commercial optical parameter amplifier (OPA) to tune its wavelength and then co-focuses with the THz beams into a ⟨110⟩-cut ZnTe crystal, to serve as a sampling beam for probing the THz waveform. After the sampling beam traverses the ZnTe crystal, it undergoes a transformation from linear to a circularly polarized beam by a quarter-wave plate. Subsequently, a Wollaston prism is employed to separate the s and p components of the circularly polarized beam. This allows for the independent measurement of the power of the two components. When no THz pulses are present, the power of the two components of the sampling beam should be "balanced," while when there is a THz pulse arriving at the ZnTe crystal simultaneously with the sampling pulse, the electric field of the THz pulse modulates the refractivity of the crystal. Consequently, the polarization state of the sampling pulse is altered, resulting in an imbalance between the two components. The difference of these two components is linearly correlated with the electric field intensity of the THz pulse, as described by the following equation:

$$S = I_0 \Gamma \sin(2\varphi), \tag{2}$$

where S is the recorded difference, I_0 is the intensity of the sampling light, φ is the angle between the direction of the polarization of the sampling light and the direction of the long axis of the index ellipsoid of the ZnTe crystal induced by the THz electric field, and Γ is the phase shift of the sampling light induced by the THz electric field when passing through the ZnTe crystal. This phase shift is directly proportional to the strength of the THz electric field. Therefore, the waveform of the THz pulses can be derived by scanning the delay line between the THz pulses and the sampling pulses. Such a method is called the electro-optical sampling (EOS). The fourth 1030 nm beam is an optional sampling beam. To sum up, a total coincidence in both time and space of all the four beams has been achieved in the ZnTe crystal and later in the STM junction.

The generated THz pulses are guided by a series of gold mirrors and off-axis parabolic (OAP) mirrors, focusing to the STM junction (through a quartz window). The whole optical path of THz pulses is completely enclosed in a N_2 atmosphere to exclude the interference from water vapor on the THz light. The system is settled in a clean room, where the temperature is maintained at around 23 °C, to guarantee the stability of the optical parts.

C. Inducing THz-driven tunneling current

The THz beam is focused onto the tunnel junction using an OAP with a focal length of 190 mm. The angle of elevation of the focusing beam is 25°. The THz spot is appropriately positioned by carefully aligning the 190 mm OAP to optimize the strength of the driven current signal. By observing the focused THz spot through a THz camera, it is evident that the minimum diameter of the focused THz spot is ~2 mm [Fig. 4(g)]. The electric field component of the THz pulses vertical to the sample surface can induce a THz-driven tunneling current. The THz-induced bias is considered to be quasi-static. This means that the THz-driven current is induced within an fs timescale, thus its direction reverses in accordance with the inverse of the THz electric field within each period. However, due to the limited BW of our control circuit and preamplifier (4 kHz), only the rectification signal of the THz-driven current can be detected. The rectification signal is greatly influenced by the waveform of the THz pulse. The opposite electric fields with similar strength within one cycle hinder the generation and detection of the rectification signal. Moreover, the nonlinearity of the I–V characteristic of the junction is essential. It should be noted that the THz pulses are generated through the optical rectification process of the $LiNbO_3$ crystal, the electric field E(t) of which satisfies formula (3),

$$E(t) \propto \chi^{(2)} \frac{\partial^2 I(t)}{\partial t^2}, \tag{3}$$

where $\chi^{(2)}$ is the second-order susceptibility and I(t) is the transient intensity of the 1030 nm pulse. Therefore, a totally linear junction would yield no rectification current.

The rectification signal is mixed with the d.c. current. To extract the rectification current signal, we use a lock-in technique. A chopper is employed to modulate the intensity of the THz pulses, with a lock-in frequency set between 500 Hz and 1 kHz, which is much lower than the repetition rate of the laser but much higher than the sampling rate of the current signal. Then, an LIA can be utilized to demodulate the specific frequency components in the current signal, enabling the extraction of the rectified THz-driven current signal. The demodulated phase is determined by various factors within the entire system, including the state of the junction, the response of the circuit, and the phase shift caused by the cables, among other influences. In many cases, the relaxation time of the sample is much shorter than the period of the chopper modulation, thus the demodulated phase remains stable as long as the experiment conditions keep unchanged. During the pump–probe experiment, both the pump and the probe beams are modulated by the chopper, resulting in the rectification signal coming from the superposition of both pulses.

The capacitance effect, namely, the charging effect, should not be neglected. The capacitance of the junction typically falls within the scale of 10^{-15} F, resulting in an impedance of 10^3 Ω at THz wavelength, while the resistance of the junction typically ranges around 10^{10} Ω, indicating that the flow of the THz-induced charges is sig-

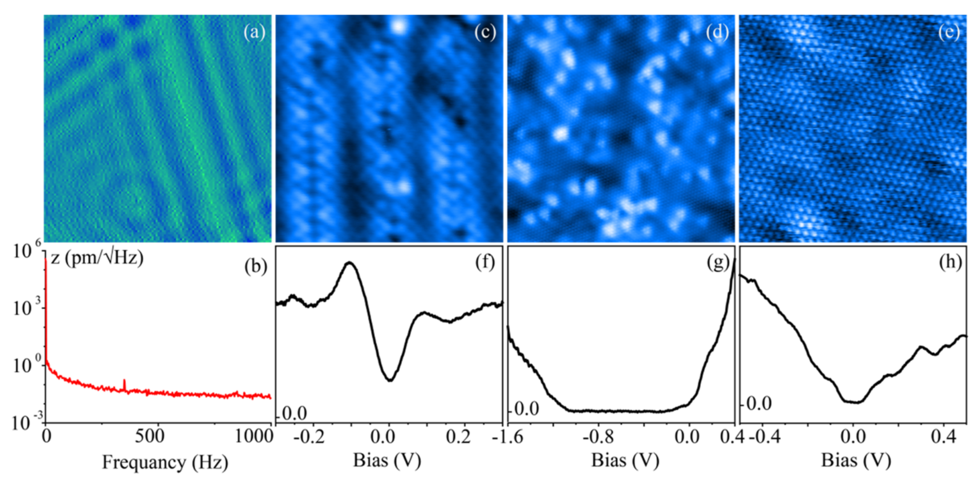

FIG. 3. STM images and spectra. (a) dI/dV mapping on Ag(111), 30 × 30 nm^2, tip bias = −20 mV, and setpoint = 500 pA. (b) Mechanical noise of the junction, in range. (c) Topography of $Bi_2Sr_2CaCu_2O_{8+\delta}$, with image size of 8 × 8 nm^2, tip bias = 600 mV, and setpoint = 30 pA. (d) Topography of GaGeTe, with image size of 30 × 30 nm^2, tip bias = 20 mV, and setpoint = 600 pA. The little dots show the hexagonal lattice of the top Te atoms, and the light-colored triangles are the defects underneath. (e) Topography of two-layer graphene/6H–SiC, with image size of 6 × 6 nm^2, tip bias = 80 mV, and setpoint = 200 pA. The larger period refers to the 6 × 6 buffer layer between graphene and SiC. (f)–(h) STS on panels (c)–(e).

nificantly stronger than the driven tunneling current. Fortunately, the flow of the induced charges does not contribute to the rectification signal, ensuring that the signal purely reflects the driven tunneling current (thus, it is reasonable to refer to the "rectification THz-driven tunneling current signal" as "driven current" or "driven signal" in the following). Although the electric field of the induced charges can cause a phase shift in the waveform of the induced bias of the junction, and the nonlinear enhancement effect of the THz electric field can lead to a distortion in the THz near-field waveform as well. Therefore, the near-field waveform differs from the far-field waveform and requires special measurement.

III. PERFORMANCE

A. STM imaging

Typical topographic and spectroscopic images obtained from our STM are shown in Fig. 3, including the topography images of cleaved $Bi_2Sr_2CaCu_2O_{8+\delta}$ (BSCCO), GaGeTe (GGT), and *in-siu* prepared bilayer graphene/SiC and their corresponding dI/dV curves, along with the dI/dV mapping of the clean Ag(111) surface. These figures demonstrate the atomic spatial resolution, clear characteristics of the surface state of Ag(111), the superconducting gap of BSCCO, the semiconductor bandgap of GGT, and spectroscopic features of graphene. The sample temperature is around 25 K, indicated by a thermocouple placed at the sample holder, and the mechanical noise of the junction has reached a level lower than 2 pm/$\sqrt{\text{Hz}}$, as shown in Fig. 3(b). It is evident that the noise level of our system is sufficiently low to satisfy the requirements for topography and STS analysis in most samples.

B. THz waveform sampling

A pyroelectric THz power meter is used to verify the generation of THz pulses. The generated THz power under different 1030 nm power levels is measured, and the results are shown in Fig. 4(a). The quadratic nonlinear relationship between powers of the THz and 1030 nm beams suggests that the collected signal is indeed generated through the optical rectification process. The polarization of

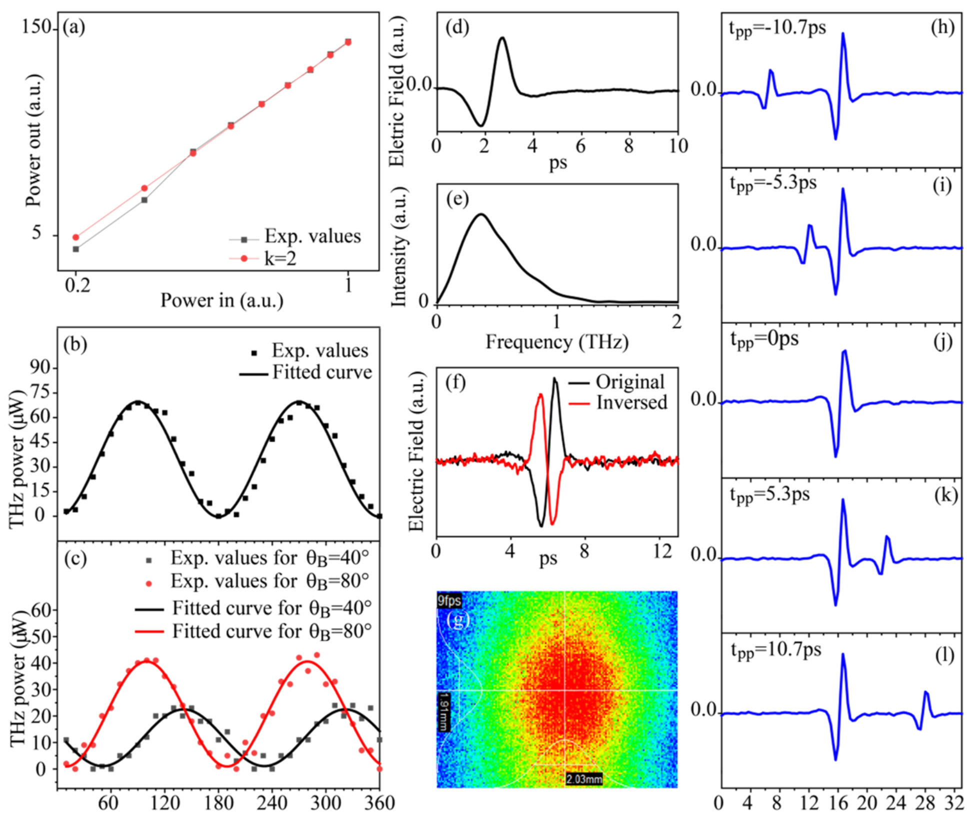

FIG. 4. Characterizations of far-field THz pulses. (a) Logarithmic graph of the power of generated THz pulses vs the power of 1030 nm pulses. The experiment values fit well with a straight line with a slope of 2. (b) Single polarizer experiment: the transmitted THz pulses shows the pattern of sinusoidal line, verifying the linear polarization of the THz pulses generated from the crystal. (c) Double polarizers experiment: the peaks of the sinusoidal pattern shift and are attenuated with the rotation of a second polarization, verifying the linear polarization of the THz pulses transmitted through the polarizer. (d) The waveform of the THz pulses by EOS. (e) The frequency spectrum of panel (d). (f) The waveform of the inverse THz pulses by EOS. (g) The THz spot captured by a THz camera in the focus inside the vacuum chamber. The diameter of the spot is down to 2 mm. (h)–(l) The waveform of double THz pulses by EOS with various time delays.

the generated linearly polarized THz pulses can be twisted by a grid polarizer. Figures 4(b) and 4(c) show the relationship between the power of the transmitted THz and the angles of the polarizers. These results confirm that both the generated THz pulses and the pulses transmitted through the polarizers exhibit linear polarization.

Another method to confirm the generation of THz pulses is the waveform sampling. The far-field waveform is shown in Figs. 4(d) and 4(e). From the waveform, we can learn that the pulse width of the THz pulses is of ps scale, and the spectrum ranges from 0.1 to 1 THz. If we take the diameter of the spot as 2 mm, an electric field peak intensity of 0.6 kV/cm can be derived. The reversed waveform is also shown in Fig. 4(f), indicating that the waveform remains relatively intact.

Figures 4(h)–4(l) show the waveform of pairs of the pump–probe pulses. Both pulses are clearly discernible, and the delay between them can be precisely controlled with an accuracy of 0.2 fs. The stronger pulse functions as the pump pulse, while the weaker pulse serves as the probe pulse.

C. THz-driven tunneling current

1. Acquisition of the driven current

The THz-driven current can be influenced by multiple factors. First, the driven current exhibits a nonlinear increase with respect to the THz intensity. This nonlinearity arises from several reasons: (1) the nonlinearity of the I–V characteristic of the junction; (2) the THz electric field induces screen charges and image charges in the metallic tip and conductive samples, enhancing the electric field in the junction, which is known as the "antenna effect;" and (3) the sharp tip further enhances the electric field in the near field, which is known as the "lightning rod effect." Second, the driven current decreases as the junction spacing increases. This effect is originated from the following reasons: (1) as the spacing increases, the nonlinear enhancement effect is weakened, leading to the decline of the induced bias and, consequently, the decrease in the driven current; (2) the probability of electron tunneling decreases as the spacing increases, which, in turn, reduces the driven current.

There are mainly two operational regimes for THz-STM, referring to the THz intensity: the tunneling regime and the emission regime. In the tunneling regime, the THz intensity is relatively weak, and the THz electric field can be viewed as a transient bias. However, when the THz intensity is increased to the point where the chemical potential of the electrons in the negative side surpasses the vacuum level in the positive side, the electrons will experience a period of motion in vacuum. In this case, the THz electric field acts as an accelerating field, causing the system to enter into the emission regime. In both regimes, the driven current increases nonlinearly with the THz intensity. The results shown in Fig. 5(a) are in accordance with this prediction.

2. Scanning imaging of the driven current

There are two commonly used operating modes of THz-STM, namely, the constant-height mode and the constant-current mode. During constant-height scanning, the tip is maintained at a fixed height, while the THz-driven current signal extracted from the LIA is recorded. This signal is determined by the local density of states (LDOS) within the transient bias. However, even if we apply a zero

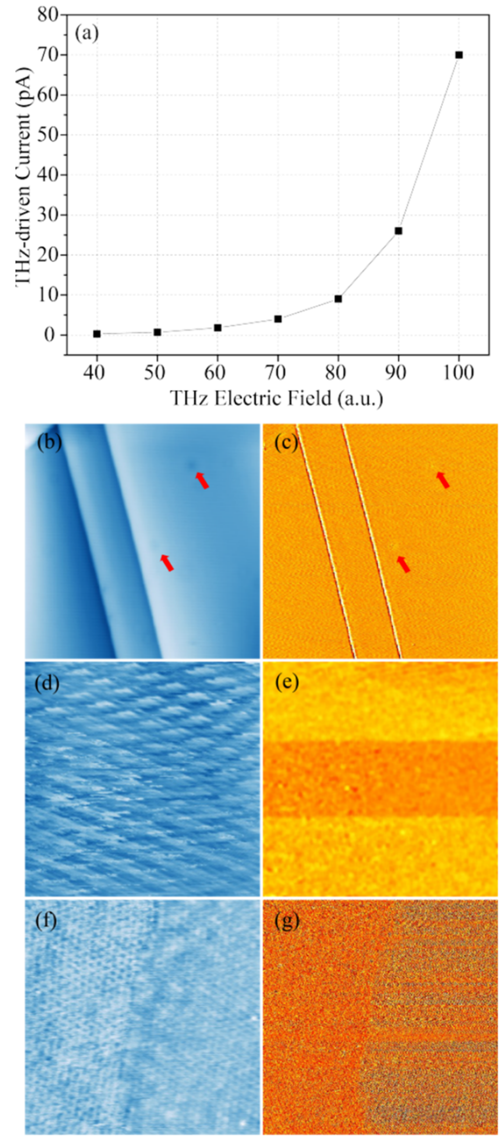

FIG. 5. Features of the THz-driven current signal. (a) The driven current is nonlinearly enhanced as the THz electric field increases. The data were acquired on Ag(111). (b) Topography of Ag(111), with size 45 × 45 nm^2, tip bias = −7 mV, and setpoint = 200 pA. (c) THz-driven current signal collected simultaneously with panel (b). Two defects appearing as dark dots in panel (b) marked by the red arrow are present on the surface, which are also visible in the THz-driven current channel, manifesting as light dots in panel (c). (d) Topography of GaGeTe, with size 4 × 4 nm^2, tips bias = 500 μV, and setpoint = 2 pA. The periodic pattern is the lattice of the surface Te atoms. (e) THz-driven current signal collected simultaneously with panel (d). No apparent signal can be observed. It should be noted that the laser was turned off when scanning to ~1/3 and then turned it back on at 2/3 of the scanning time, to verify that the signal is indeed THz-driven. (f) Topography of few-layer graphene/SiC, 50 × 50 nm^2, tip bias = 1 mV, and setpoint = 200 pA. The periodic pattern is the lattice of the 6 × 6 buffer layer. In the image, the left side is covered by mono-layer graphene, while the right side is covered by bilayer graphene. (g) THz-driven current signal collected simultaneously with panel (f). The bilayer region shows a stronger signal than the mono-layer region. The disappearing scanning lines in the image are due to intentionally turning off the laser during those instances to verify that the signal is indeed THz-driven.

d.c. bias, the presence of contact electromotive force (emf) and thermal-emf causes the persistence of a d.c. current. Consequently, the driven current becomes mixed with the d.c. current, making its extraction difficult. Conversely, during constant-current scanning, the height of the tip is adjusted to maintain a setpoint for the current signal. The driven current signal is simultaneously impacted by both LDOS and the junction spacing. The junction spacing is mainly determined by the d.c. current. Therefore, the driven current is inevitable influenced by the d.c. current. In conclusion, both constant-height and constant-current modes possess advantages and disadvantages, necessitating a comprehensive analysis.

Figure 5 shows the selected scanning imaging results obtained using the driven current signal in the constant-current mode. The driven current image on Ag(111) is shown in Fig. 5(c). Defects are manifested as light dots in the image, indicated by the red arrows. When the tip is positioned over these defects, the reduction of the junction spacing leads to an increase in the THz-driven signal, corresponding to the bright dots signals. Figure 5(e) shows the driven current image on cleaved GaGeTe, which is a kind of layered semiconductor. In Fig. 5(g), we also show the driven current image on few-layer graphene/SiC. It can be found that the signal on bilayer graphene is stronger than that on mono-layer, which can be explained to be originated from the surface charge density difference. We found that the THz-driven signal on GaGeTe, FeSe (see below), and epitaxial graphene is weak, typically at the order of 100 fA, in contrast to bulk materials, such as Au(111), Ag(111), and Si(111), where the driven signal is able to reach tens of pA. It could thus be inferred that the THz-driven signal would be weaker on layered materials, probably because of the lower carrier density and the weaker inter-layer transferring within the range of the penetration depth of the THz electric field.

3. Temporal resolution

The THz pump–THz probe configuration enables detection of the driven current with temporal resolution. Due to the nonlinearly enhancement of the THz electric field, when a pump pulse and a probe pulse arrive at the junction simultaneously, the driven signal undergoes an extra amplification known as the "autocorrelation" signal. The full width at half maximum (FWHM) of this signal is considered as the time resolution of the driven current. It is shown in Fig. 6(a) that the system achieves a time resolution of 700 fs. The delay stage moves continuously at a speed of 0.04 mm/s, corresponding to a uniform change in the delay time between the two pulses at a rate of 267 fs/s. The sampling rate of the z-channel signal is 50 Hz, which is equivalent to sampling a point approximately every 50 fs.

4. Spatial resolution

Thanks to the near-field enhancement of the THz electric field by the STM tip, the driven current exhibits a high spatial resolution capability. Figure 6(i) shows the driven current collected on the Si(111) 7 × 7 reconstruction surface using constant-height mode. The distinct visibility of the surface atoms demonstrates the high spatial resolution ability of the technique. Figures 6(j) and 6(k) show the simultaneous collection of an STM image and a driven current image on a single crystal of FeSe. The FeSe surface was prepared *in situ* through cleaving and verified using STM topography. As shown in Fig. 6(j), the orthorhombic lattice in the STM image is the signal of the top Se atoms. The four-lobe protrusion corresponds to a single Se atom defect.[40] The defect marked by the red arrow is attributed to a single Fe atom vacancy,[41] which is less discernible

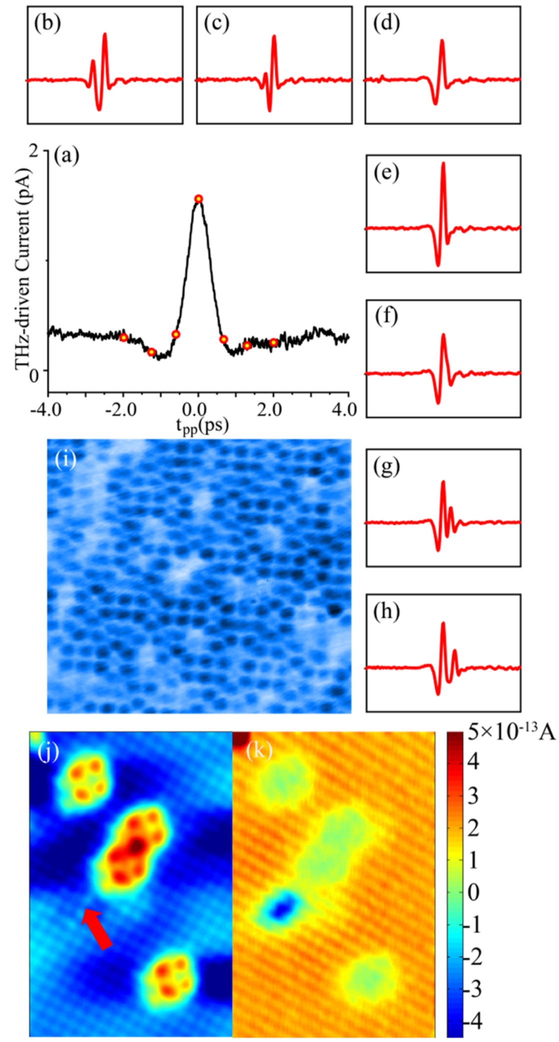

FIG. 6. Time resolution and spatial resolution of the THz-driven current. (a) The autocorrelation signal derived on Ag(111) with feedback off. (b)–(h) The waveform of double THz pulses corresponding to the red indicating points in panel (a) sequentially, among which panel (e) shows the waveform at zero time delay. (i) Scanning imaging using THz-driven current on the Si(111) 7 × 7 reconstruction surface under constant-height mode, 10 × 12 nm^2, where tip bias is set to 0 V and the total current is around 30 pA. An atomic spatial resolution is achieved. (j) Topography of FeSe under constant-current mode, 9 × 6 nm^2, tip bias = 3 mV, and setpoint = 30 pA. The orthorhombic lattice is the signal of the top Se atoms. The single Se atom vacancies are manifested as the four-lobe protrusions, while the single Fe atom vacancy is less discernible under this specific scan condition, which is marked by the red arrow. (k) THz-driven current signal collected simultaneously with panel (j). The driven signal decreases around the Se defects, exhibiting a concave shape, while it inverses around the Fe defects, appearing as a highly pronounced concavity.

under this specific scan condition. While in the driven current image [Fig. 6(k)], the driven signal decreases significantly around the Se defects compared to the background, exhibiting a concave shape. In contrast, around the Fe defects, the driven signal shows an inverse increase, manifesting as negative values and appearing as a highly pronounced concavity in the image. These behaviors of both the Fe defects and Se defects are notably distinct from those observed in the topographic channel shown in Fig. 6(j). This phenomenon may provide valuable insights into the LDOS and other information related to the defects. Detailed analysis requires further experiments and calculations.

IV. CONCLUSION

In conclusion, we have designed and built a cryogen-free LT THz-STM system that combines atomic-level spatial resolution with sub-ps level time resolution. This system features a very compact UHV chamber that can locate the optical part completely outside the chamber and greatly improves the convenience of optical coupling.

Countless materials have proven to be responsive to THz pulses. For instance, a variety of collective modes in superconductors has been researched using ultrafast THz techniques, but has seldom been visualized in spatial dimensions yet.[42–44] The electron dynamics in certain ferroelectric, ferromagnetic, and multiferroic materials have exhibited notable THz response,[45–47] and it is anticipated that some intriguing experimental phenomenon can be observed using THz-STM. In addition, novel phases, such as charge density wave (CDW), spin density wave (SDW), or the Moiré superlattice, in some multilayer structures renormalize the energy structure into smaller scales, enabling the possibilities to be coupled with THz excitation. Moreover, experiments have indicated the capability of THz electric fields to drive carriers within diverse material systems.[48–50] Our THz-STM system is expected to play a role in these research areas.

ACKNOWLEDGMENTS

This work was supported by the National Natural Science Foundation of China under Grant No. 1192780039.

AUTHOR DECLARATIONS

Conflict of Interest

The authors have no conflicts to disclose.

Author Contributions

Huaiyu Zhang: Data curation (equal); Investigation (equal); Writing – original draft (equal). **Dacheng Tian**: Investigation (equal). **Yang Zhan**: Investigation (equal). **Zijia Liu**: Investigation (equal). **Chen Ma**: Data curation (equal). **Yuwu Zhang**: Investigation (equal). **Jianwei Hu**: Investigation (equal). **Xiaoyue He**: Investigation (equal). **Baojie Feng**: Supervision (equal). **Yiqi Zhang**: Supervision (equal). **Lan Chen**: Supervision (equal). **Peng Cheng**: Investigation (equal); Supervision (equal); Writing – review & editing (equal). **Kehui Wu**: Conceptualization (equal); Funding acquisition (equal); Investigation (equal); Methodology (equal); Project administration (equal); Supervision (equal); Writing – review & editing (equal).

DATA AVAILABILITY

The data that support the findings of this study are available from the corresponding authors upon reasonable request.

REFERENCES

[1] Y. Tian, F. Yang, C. Guo, and Y. Jiang, Surf. Rev. Lett. **25**, 1841003 (2018).
[2] G. Schitter and M. J. Post, Mater. Today **11**, 40 (2008).
[3] P. A. Sloan, J. Phys.: Condens. Matter **22**, 264001 (2010).
[4] S. Weiss, D. F. Ogletree, D. Botkin, M. Salmeron, and D. S. Chemla, Appl. Phys. Lett. **63**, 2567 (1993).
[5] O. Takeuchi, M. Aoyama, R. Oshima, Y. Okada, H. Oigawa, N. Sano, H. Shigekawa, R. Morita, and M. Yamashita, Appl. Phys. Lett. **85**, 3268 (2004).
[6] P. Kloth, T. Thias, O. Bunjes, J. von der Haar, and M. Wenderoth, Rev. Sci. Instrum. **87**, 123702 (2016).
[7] T. L. Cocker, V. Jelic, M. Gupta, S. J. Molesky, J. A. Burgess, G. D. L. Reyes, L. V. Titova, Y. Y. Tsui, M. R. Freeman, and F. A. Hegmann, Nat. Photonics **7**, 620 (2013).
[8] T. L. Cocker, D. Peller, P. Yu, J. Repp, and R. Huber, Nature **539**, 263 (2016).
[9] D. Peller, C. Roelcke, L. Z. Kastner, T. Buchner, A. Neef, J. Hayes, F. Bonafe, D. Sidler, M. Ruggenthaler, A. Rubio *et al.*, Nat. Photonics **15**, 143 (2020).
[10] D. Peller, L. Z. Kastner, T. Buchner, C. Roelcke, F. Albrecht, N. Moll, R. Huber, and J. Repp, Nature **585**, 58 (2020).
[11] V. Jelic, K. Iwaszczuk, P. H. Nguyen, C. Rathje, G. J. Hornig, H. M. Sharum, J. R. Hoffman, M. R. Freeman, and F. A. Hegmenn, Nat. Phys. **13**, 591 (2017)
[12] Y. Luo, V. Jelic, G. Chen, P. H. Nguyen, Y. J. R. Liu, J. A. M. Calzada, D. J. Mildenberger, and F. A. Hegmann, Phys. Rev. B **102**, 205417 (2020).
[13] K. Yoshida, I. Katayama, Y. Minami, M. Kitajima, S. Yoshida, H. Shigekawa, and J. Takeda, Nat. Photonics **10**, 762 (2016).
[14] K. Yoshioka, I. Katayama, Y. Arashida, A. Ban, Y. Kawada, K. Konishi, H. Takahashi, and J. Takeda, Nano Lett. **18**, 5198 (2018).
[15] K. Kimura, Y. Morinaga, H. Imada, I. Katayama, K. Asakawa, K. Yoshioka, Y. Kim, and J. Takeda, ACS Photonics **8**, 982 (2021).
[16] L. Wang, Y. Xia, and W. Ho, Science **376**, 401 (2022).
[17] L. Wang, D. Bai, Y. Xia, and W. Ho, Phys. Rev. Lett. **130**, 096201 (2023).
[18] Y. Xia, L. Wang, and W. Ho, Phys. Rev. Lett. **132**, 076903 (2024).
[19] S. Chen, W. Shi, and W. Ho, Nano Lett. **23**, 2915 (2023).
[20] Y. Xia, L. Wang, D. Bai, and W. Ho, ACS Nano **17**, 23144 (2023).
[21] M. Abdo, S. Sheng, S. Rolf-Pissarczyk, L. Arnhold, J. A. J. Burgess, M. Isobe, L. Malavolti, and S. Loth, ACS Photonics **8**, 702 (2021).
[22] S. Sheng, A. Oeter, M. Abdo, K. Lichtenberg, M. Hentschel, and S. Loth, Phys. Rev. Lett. **129**, 043001 (2022).
[23] S. Yoshida, H. Hirori, T. Tachizaki, K. Yoshioka, Y. Arashida, Z. Wang, Y. Sanari, O. Takeuchi, Y. Kanemitsu, and H. Shigekawa, ACS Photonics **6**, 1356 (2019).
[24] S. Yoshida, Y. Arashida, H. Hirori, T. Tachizaki, A. Taninaka, H. Ueno, O. Takeuchi, and H. Shigekawa, ACS Photonics **8**, 315 (2021).
[25] H. Q. Nguyen, P. H. Cutler, T. E. Feuchtwang, Z. Huang, Y. Kuk, P. J. Silverman, A. A. Lucas, and T. E. Sullivan, IEEE Trans. Electron Devices **36**, 2671 (1989).
[26] E. H. Hauge and J. A. Stovneng, Rev. Mod. Phys. **61**, 917 (1989).
[27] M. Garg and K. Kern, Science **367**, 411 (2020).
[28] R. Zhang, Y. Zhang, Z. C. Dong, S. Jiang, C. Zhang, L. G. Chen, L. Zhang, Y. Liao, J. Aizpurua, Y. Luo, J. L. Yang, and J. G. Hou, Nature **498**, 82 (2013).
[29] R. Berndt, J. K. Gimzewski, and P. Johansson, Phys. Rev. Lett. **67**, 3796 (1991).
[30] L. Wimmer, G. Herink, D. R. Solli, S. V. Yalunin, K. E. Echternkamp, and C. Robers, Nat. Phys. **10**, 432 (2014).
[31] M. Muller, N. M. Sabanes, T. Kampfrath, and M. Wolf, ACS Photonics **7**, 2046 (2020).

[32]T. L. Cocker, V. Jelic, R. Hillenbrand, and F. A. Hegmann, Nat. Photonics **15**, 558 (2021).
[33]S. E. Ammerman, Y. Wei, N. Everett, V. Jelic, and T. L. Cocker, Phys. Rev. B **105**, 115427 (2022).
[34]I. Katayama, K. Kimura, H. Imada, Y. Kim, and J. Takeda, J. Appl. Phys. **133**, 110903 (2023).
[35]J. Allerbeck, J. Kuttruff, L. Bobzien, L. Huberich, M. Tsarev, and B. Schuler, ACS Photonics **10**, 3888 (2023).
[36]H. Li, T. Wang, W. Wei, K. Zhang, J. Xu, Y. Wu, and G. Fang, ACS Photonics **11**, 1428 (2024).
[37]L. Bobzien, J. Allerbeck, S. E. Ammerman, R. Torsi, J. A. Robinson, and B. Schuler, APL Mater. **12**, 051110 (2024).
[38]H. Azazoglu, P. Kapitza, M. Mittendorff, R. Moller, and M. Gruber, Rev. Sci. Instrum. **95**, 023703 (2024).
[39]R. Ma, H. Li, C. Shi, F. Wang, L. Lei, Y. Huang, Y. Liu, H. Shan, L. Liu, S. Huang *et al.*, Rev. Sci. Instrum. **94**, 093701 (2023).
[40]C. Song, Y. Wang, P. Cheng, Y. Jiang, W. Li, T. Zhang, Z. Li, K. He, L. Wang, J. Jia *et al.*, Science **332**, 1410 (2011).
[41]K. Bu, B. Wang, W. Zhang, Y. Fei, Y. Zheng, F. Ai, Z. Wu, Q. Wang, H. Wo, J. Zhao *et al.*, Phys. Rev. B **100**, 155127 (2019).
[42]R. Ulbricht, E. Hendry, J. Shan, T. F. Heinz, and M. Bonn, Rev. Mod. Phys. **83**, 543 (2011).
[43]R. Matsunaga, Y. I. Hamada, K. Makise, Y. Uzawa, H. Terai, Z. Wang, and R. Shimano, Phys. Rev. Lett. **111**, 057002 (2013).
[44]S. Kovalev, T. Dong, L. Shi, C. Reinhoffer, T. Xu, H. Wang, Y. Wang, Z. Gan, S. Germanskiy, J. Deinert *et al.*, Phys. Rev. B **104**, L140505 (2021).
[45]J. Lu, X. Li, H. Y. Hwang, B. K. Ofori-Okai, T. Kurihara, T. Suemoto, and K. A. Nelson, Phys. Rev. Lett. **118**, 207204 (2017).
[46]X. Li, T. Qiu, J. Zhang, E. Baldini, J. Lu, A. M. Rappe, and K. A. Nelson, Science **364**, 1079 (2019).
[47]T. Kubacka, J. A. Johnson, M. C. Hoffmann, C. Vicario, S. de Jong, P. Beaud, S. Grubel, S. Huang, L. Huber, L. Patthey *et al.*, Science **343**, 1333 (2014).
[48]F. Junginger, B. Mayer, C. Schmidt, O. Schubert, S. Mahrlein, A. Leitenstorfer, R. Huber, and A. Pashkin, Phys. Rev. Lett. **109**, 147403 (2012).
[49]J. Reimann, S. Schlauderer, C. P. Schmid, F. Langer, S. Baierl, K. A. Kokh, O. E. Tereshchenko, A. Kimura, C. Lange, J. Gudde *et al.*, Nature **562**, 396 (2018).
[50]H. A. Hafez, S. Kovalev, J. Deinert, Z. Mics, B. Green, N. Awari, M. Chen, S. Germanskiy, U. Lehnert, J. Teichert *et al.*, Nature **561**, 507 (2018).